nature nanotechnology

ARTICLES

PUBLISHED ONLINE: 10 JULY 2017 | DOI: 10.1038/NNANO.2017.129

# Air-stable and freestanding lithium alloy/graphene foil as an alternative to lithium metal anodes

Jie Zhao[1†], Guangmin Zhou[1†], Kai Yan[1], Jin Xie[1], Yuzhang Li[1], Lei Liao[1], Yang Jin[1], Kai Liu[1], Po-Chun Hsu[1], Jiangyan Wang[1], Hui-Ming Cheng[2,3] and Yi Cui[1,4*]

**Developing high-capacity anodes is a must to improve the energy density of lithium batteries for electric vehicle applications. Alloy anodes are one promising option, but without pre-stored lithium, the overall energy density is limited by the low-capacity lithium metal oxide cathodes. Recently, lithium metal has been revived as a high-capacity anode, but faces several challenges owing to its high reactivity and uncontrolled dendrite growth. Here, we show a series of Li-containing foils inheriting the desirable properties of alloy anodes and pure metal anodes. They consist of densely packed $Li_xM$ (M = Si, Sn, or Al) nanoparticles encapsulated by large graphene sheets. With the protection of graphene sheets, the large and freestanding $Li_xM$/graphene foils are stable in different air conditions. With fully expanded $Li_xSi$ confined in the highly conductive and chemically stable graphene matrix, this $Li_xSi$/graphene foil maintains a stable structure and cyclability in half cells (400 cycles with 98% capacity retention). This foil is also paired with high-capacity Li-free $V_2O_5$ and sulfur cathodes to achieve stable full-cell cycling.**

The emerging market of electric vehicles has stimulated intensive research on lithium-ion (Li-ion) batteries with high energy density and long cycle life[1,2]. Conventional anodes, primarily based on graphite with a theoretical capacity of 370 mAh $g^{-1}$, struggle to completely fulfil the demand[3]. Alloy anodes with much higher theoretical capacity (for example, Si: 4,200 mAh $g^{-1}$; Sn: 990 mAh $g^{-1}$; and SiO: 2,670 mAh $g^{-1}$) have been widely recognized as promising alternatives for high energy density applications[4]. However, because of their large volume change during lithiation–delithiation, these alloy anodes may potentially suffer from mechanical disintegration of the electrode structure and instability of the solid electrolyte interphase[5,6]. Diverse micro- and nanostructure designs have been utilized to address these problems, achieving long-term cycling with high capacity[7,8]. Particularly, freestanding Si/C composite films were fabricated to realize lightweight electrodes with further improved electrochemical performance[9–11]. However, alloy anodes are free of Li and are typically paired with low-capacity Li metal oxide cathode materials (<200 mAh $g^{-1}$), which significantly limits the energy density of Li-ion batteries[12,13]. Generally, Li-free cathode materials (for example, sulfur: 1,672 mAh $g^{-1}$; $V_2O_5$: 441 mAh $g^{-1}$) have much higher specific capacity[14–16]. As a result, there is a strong motivation to develop a new full-cell configuration with a Li-containing anode[17].

Li metal is an attractive anode to construct full cells with Li-free cathodes because of its high specific capacity of 3,860 mAh $g^{-1}$ and lowest electrochemical potential (−3.04 V versus the standard hydrogen electrode)[18,19]. However, Li metal anodes raise serious safety concerns and have a low Coulombic efficiency (CE) due to their uncontrolled dendrite formation, relative infinite volume change during Li plating and stripping, and high chemical reactivity with organic electrolytes[20–22]. Extensive works, including Li/3D matrix composites[23,24], electrolyte additives[25,26], mechanically and chemically stable interphase[27,28] and spatial deposition control[29], have significantly suppressed dendrite formation and pushed the CE in corrosive carbonate electrolytes up to 98%. However, this technology is still far from real applications.

In addition, the use of Li metal is challenging because of its demanding processing requirements. Li metal is corroded immediately on exposure to humid air[30]. Li metal anodes with fine structures typically show improved electrochemical performance and worsened stability associated with their enlarged surface area. Coating Li microparticles with $Li_2CO_3$ has been employed to enhance the stability of the lithium metal, but the use of a costly dry room is necessary[31,32]. Other coatings such as $Al_2O_3$ via atomic layer deposition improves the stability under ambient conditions (40% relative humidity)[30]. However, the surface texture of Li metal changes after the air exposure for several hours. An air-stable, Li-containing anode with long-term cycling stability and high CE is therefore highly desired.

Here, we report a facile process to fabricate large-scale and freestanding $Li_xM$/graphene foils (M = Si, Sn, or Al) with the unique nanostructure of densely packed reactive $Li_xM$ nanoparticles encapsulated by large graphene sheets (graphene refers to few-layer (<10 layers) graphene). The volumetric capacity of the $Li_xSi$/graphene foil is 1,800–2,000 mAh $cm^{-3}$, approaching the theoretical value of Li metal (2,061 mAh $cm^{-3}$)[33]. With fully expanded $Li_xSi$ confined in the graphene matrix, the foil avoids the intrinsic problems of volume expansion and dendrite growth that plague Li metal, exhibiting stable cycling (400 cycles with 98% capacity retention) at areal capacity of ~2.4 mAh $cm^{-2}$ in half cells. The $Li_xSi$/graphene foil is successfully paired with Li-free cathodes ($V_2O_5$ and sulfur) to achieve stable full-cell cycling. The cells are in the charged state after assembly, delivering an estimated energy density of ~500 Wh $kg^{-1}$. The excellent air-stability of $Li_xM$/graphene foils is attributed to their unique structure where each $Li_xM$ cluster is completely surrounded and

[1]Department of Materials Science and Engineering, Stanford University, Stanford, California 94305, USA. [2]Shenyang National Laboratory for Materials Science, Institute of Metal Research, Chinese Academy of Sciences, 72 Wenhua Road, Shenyang 110016, People's Republic of China. [3]Tsinghua-Berkeley Shenzhen Institute, Tsinghua University, 1001 Xueyuan Road, Shenzhen 518055, People's Republic of China. [4]Stanford Institute for Materials and Energy Sciences, SLAC National Accelerator Laboratory, 2575 Sand Hill Road, Menlo Park, California 94025, USA. †These authors contributed equally to this work. *e-mail: yicui@stanford.edu

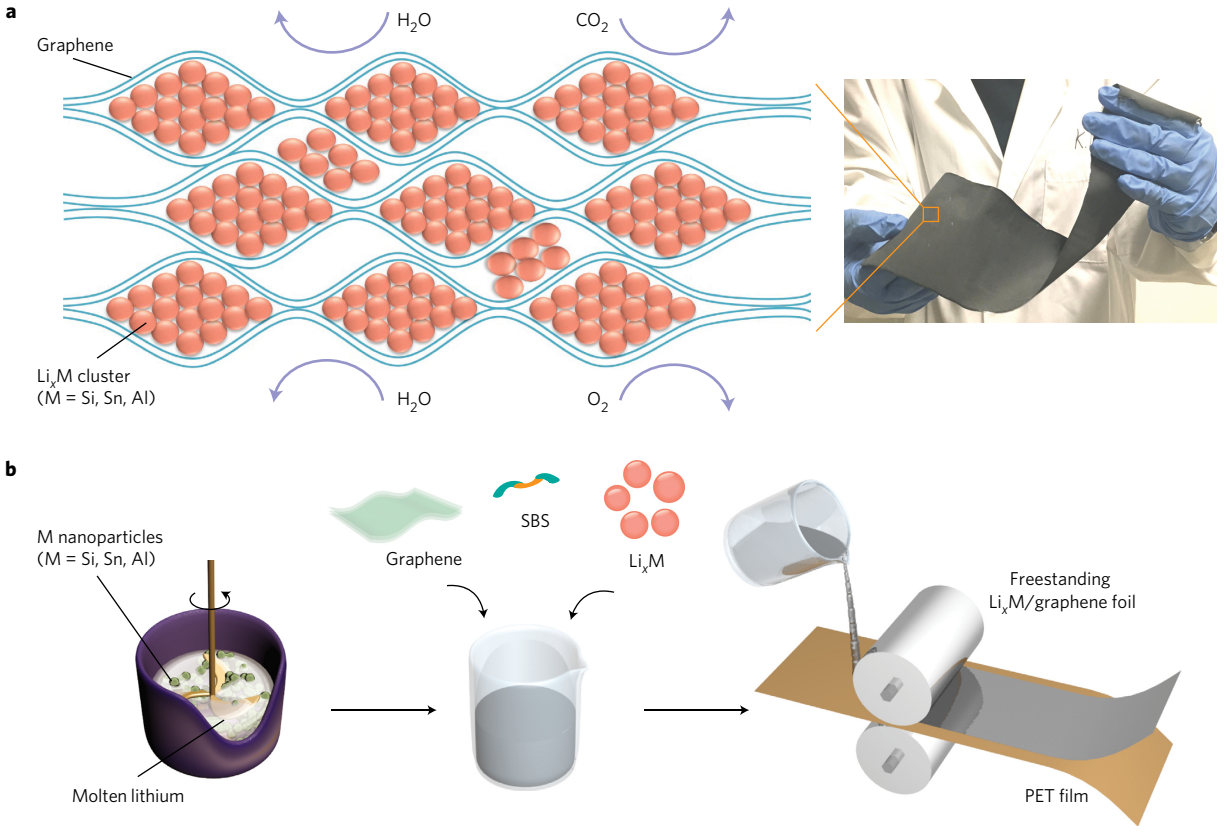


**Figure 1 | Schematic of the microstructure and fabrication process of the $Li_xM$/graphene foils. a**, Schematic illustrating the unique foil structure comprising densely packed reactive $Li_xM$ nanoparticles encapsulated by large graphene sheets. M refers to Si, Sn, or Al, but other materials that can form alloys with Li can potentially be used. This foil is highly stable in different air conditions thanks to its unique structure as well as the hydrophobicity and gas impermeability of graphene sheets. The photograph of a large $Li_xSi$/graphene foil shows its good flexibility and the potential to scale up to industrial fabrication. **b**, $Li_xM$ nanoparticles were synthesized by heating a stoichiometric mixture of M nanoparticles and Li metal under mechanical stirring in an argon atmosphere. $Li_xM$ nanoparticles were mixed with graphene sheets and SBS rubber (80:10:10 by weight) to form a slurry, which was then cast on a PET release film. After drying, it was peeled off as a large freestanding $Li_xM$/graphene foil.

protected by the large graphene sheets. Theoretically, the hydrophobicity[34,35] and gas impermeability[36] of the graphene sheets prevent the absorption and penetration of gas molecules.

## Fabrication and characterization of the $Li_xM$/graphene foil

We have developed a scalable approach to fabricate a $Li_xSi$/graphene foil (Fig. 1). Similar to our previous study, $Li_xSi$ nanoparticles were synthesized on the gram-scale, by heating a stoichiometric mixture of Li metal and Si nanoparticles under mechanical stirring in an argon glovebox[37]. $Li_xSi$ nanoparticles were mixed with graphene sheets and poly(styrene-butadiene-styrene) (SBS) rubber (80:10:10 by weight) in toluene to form a slurry, which was then casted on a polyethylene terephthalate (PET) release film. After drying, the $Li_xSi$/graphene can be easily peeled off as a large freestanding foil. Thin layers of graphene sheets were coated on the double sides of the foil to ensure that even the $Li_xSi$ nanoparticles on the surface were fully protected. This foil preparation process is also applicable to other Li alloy forming materials, such as Al and Sn. Figure 2a shows a large $Li_xSi$/graphene foil (8 cm wide and 24 cm long). Supplementary Movie 1 shows the foil being rolled on a tube with a diameter of 3 mm and then being unfolded without any damage. The superior mechanical property of the $Li_xSi$/graphene foil is further demonstrated by the uniaxial tensile test, which shows a similar trend to a Li metal foil with much higher stress (Fig. 2d). $Li_xSi$/graphene can also be coated on two sides of a copper foil to form an electrode similar to the one used in cylindrical cells (Supplementary Fig. 1).

The graphene sheets were prepared by exfoliation of graphite with the assistance of metal halide[38]. A low-magnification transmission electron microscopy (TEM) image (Fig. 2b) shows overlapped and interconnected graphene sheets up to several micrometres. A double-layer graphene is clearly observed in Fig. 2c, with an average interlayer distance of 0.334 nm (Supplementary Fig. 2a). The TEM image in Supplementary Fig. 2b shows graphene sheets with 3–6 layers. Raman spectroscopy analysis also suggests multilayer graphene (Supplementary Fig. 2c)[39]. The D to G peak intensity ratio ($I_D/I_G = 0.05$) indicates a low concentration of defects in graphene[40]. The quality of graphene is further confirmed by X-ray photoelectron spectroscopy (XPS) (Supplementary Fig. 2d), showing extremely low oxygen content. The X-ray diffraction (XRD) pattern (Fig. 2e) of the $Li_xSi$/graphene foil contains peaks of $Li_{22}Si_5$ (powder diffraction file (PDF) no. 01-077-2882), graphitic carbon (PDF no. 00-056-0159) and $Li_2O$ (PDF no. 04-008-3420). $Li_xSi$ nanoparticles are identifiable underneath the thin graphene sheet (Fig. 2f). The $Li_xSi$ alloy is already in its fully expanded state, so no void space needs to be created to accommodate the volume expansion of Si. Accordingly, the $Li_xSi$/graphene foil can be thoroughly calendared without damaging its microstructures. After calendaring at large stress of 40 MPa, $Li_xSi$ nanoparticles are in a densely packed state as shown in the cross-sectional SEM image (Fig. 2g).

## Stability of the $Li_xSi$/graphene foil

Theoretically, the gas impermeability of graphene, and the hydrophobicity of graphene and the SBS rubber could improve the

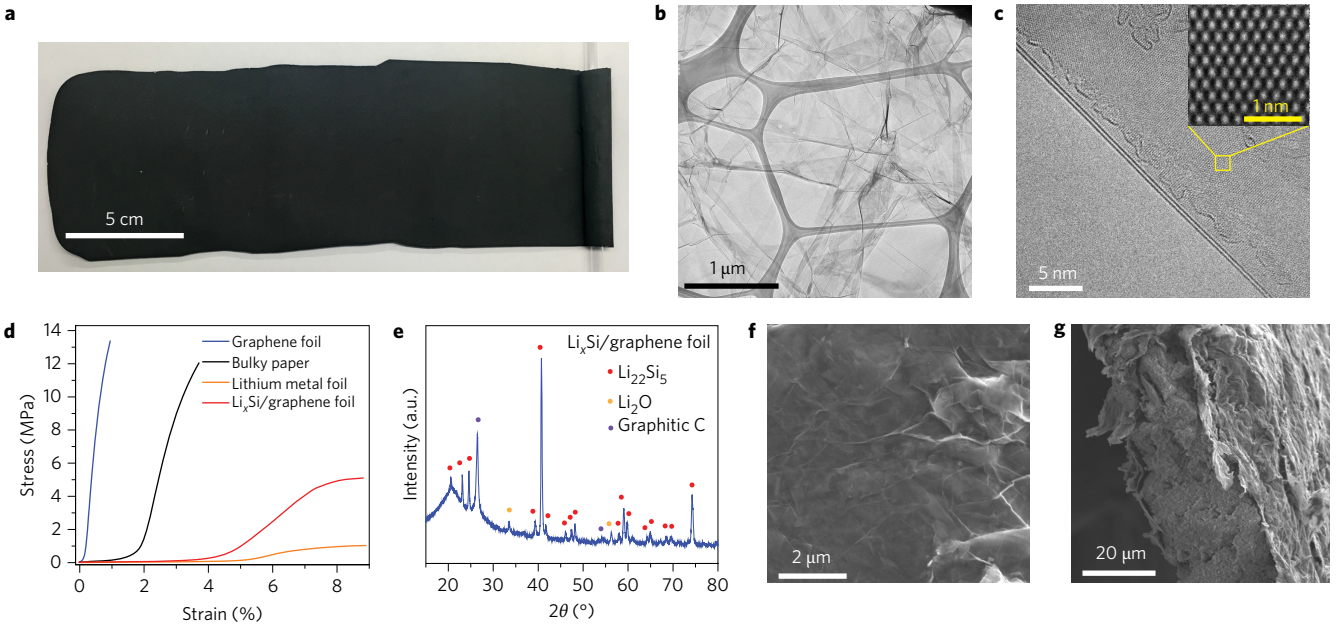


**Figure 2 | Characterization of the $Li_xSi$/graphene foil. a**, Photograph of a large $Li_xSi$/graphene foil with 8 cm width and 24 cm length. The right side of the foil is rolled around a thin tube to illustrate its good flexibility. **b**, Low-magnification TEM image of the overlapped and interconnected graphene sheets. **c**, TEM image shows a double-layer graphene sheet with an interlayer distance of 0.334 nm. The inset is an atomic-resolution image of the graphene sheet. **d**, Uniaxial tensile tests of the graphene foil, bulky paper, Li metal foil and $Li_xSi$/graphene foil. **e**, XRD pattern reveals the highly crystalline nature of graphitic carbon and $Li_{22}Si_5$. **f**,**g**, Top-view (**f**) and cross-sectional view (**g**) SEM images of the $Li_xSi$/graphene foil.

stability of the $Li_xSi$/graphene foil. A water drop placed on top of a pure graphene foil gives a contact angle of 93.1° (Fig. 3a). SBS is dissolved in toluene and then spin-coated on a Si wafer. The contact angle of 99.9° confirms the hydrophobicity of SBS. After being dispersed in the SBS/toluene solution for 2 h, $Li_xSi$ nanoparticles are enwrapped by a ~40-nm-thick coating (Supplementary Fig. 3). Theoretically, graphene is impermeable to gases and robust against oxidation (Fig. 3b, top), suggesting that few-layer graphene sheets are effective anti-corrosion barriers[36]. The hydrophobic nature repels the water molecules. Furthermore, the gas impermeability nature ensures that the graphene sheets can prevent gas penetration, even if the molecules in the air are adsorbed on the foil. The cross-sectional SEM image (Fig. 3b, bottom) shows that the $Li_xSi$ nanoparticles aggregate to form a cluster during calendaring and that the cluster is perfectly encapsulated by the graphene sheets. Therefore, each $Li_xSi$ cluster is entirely protected by the graphene sheets. Photographs of the Li foil and the $Li_xSi$/graphene foil exposed to ambient air (daytime relative humidity = 20–30%, night time relative humidity = 50–60%) indicate the superior stability of the $Li_xSi$/graphene foil (Fig. 3c). After exposure to ambient air for just 3 min, the colour of Li metal turns black. The XPS analysis (Supplementary Fig. 4) indicates the formation of $Li_2CO_3$ after 48 h exposure[41]. The colour of $Li_xSi$/graphene foil remains the same even after 48 h. The cross-sectional SEM images (Supplementary Fig. 5a,b) confirm that the change in thickness is negligible after exposure to ambient air for 1 day. To test whether the foil is stable for the baking process, the foil with 19-μm thickness was baked at 80 °C for 6 h in the dry room (dew point, −50 °C). The areal capacity of the $Li_xSi$/graphene foil remained almost unchanged, indicating that this foil can survive the baking process to remove residual solvent and water (Fig. 3d). To investigate the dry-air stability, the foil was stored in the dry room for two weeks and its remaining capacity was examined over time. After two weeks, it still maintained 94.3% of its original capacity, exhibiting a high areal capacity of 3.6 mAh $cm^{-2}$ (Fig. 3e). XRD confirms that there was no obvious change after dry-air exposure (Supplementary Fig. 6a,b). Nanoscale Li alloy is extremely unstable in ambient air, losing most of its capacity within just several hours (Fig. 3f inset). With the protection of the graphene sheets, the $Li_xSi$/graphene foil exhibits excellent stability even in air with a high humidity level (20–60% relative humidity). After being exposed to ambient air for 3 days, the foil still exhibits a high areal capacity of 3.1 mAh $cm^{-2}$ (Fig. 3f). The XRD pattern reveals small peaks belonging to LiOH (PDF no. 00-032-0564), which is related to $H_2O$ contamination in the humid air (Supplementary Fig. 6c). Rietveld refinement quantitative analysis confirms that $Li_{22}Si_5$ remains the main component. With a lower amount of graphene, the foil ($Li_xSi$:graphene:SBS = 90:5:5 by weight) exhibits a large capacity drop (42%) after exposure to the ambient air for the same time (Supplementary Fig. 7). The air stability of the $Li_xSi$/graphene foil increases the possibility for safe handling and simplifies the requirements on the industrial battery fabrication environment.

## Electrochemical performance of the $Li_xSi$/graphene foil

The first-cycle delithiation capacities of $Li_xSi$/graphene foils with thicknesses of 19 and 42 μm were 3.8 and 8.3 mAh $cm^{-2}$ in half cells, respectively (Fig. 4a and Supplementary Fig. 8). Based on the foil thickness and areal capacity, the volumetric capacity is ~2,000 mAh $cm^{-3}$, close to the theoretical value of $Li_{22}Si_5$ (2,240 mAh $cm^{-3}$) and Li (2,061 mAh $cm^{-3}$)[4,33]. The experimental values for Si anodes reported in the literature are generally lower than 1,300 mAh $cm^{-3}$ due to the low tap density of nanostructured Si and void space created to accommodate the volume expansion[8]. The specific capacity of the $Li_xSi$/graphene foil is ~1,600 mAh $g^{-1}$ based on the mass of $Li_xSi$. The foils with thicknesses of 12 and 19 μm are used to evaluate the long-term cycling performance (Fig. 4b). From the 4th to the 400th cycle at a current density of 1 mA $cm^{-2}$, the capacity retention of the 19-μm-thick foil is ~98%, showing an areal capacity of 2.4 mAh $cm^{-2}$. There are two characteristics that allow for such superior cycling performance. The first is the high conductivity of graphene sheets (1,400 S $cm^{-1}$). The second is that Si is already in its fully lithiated

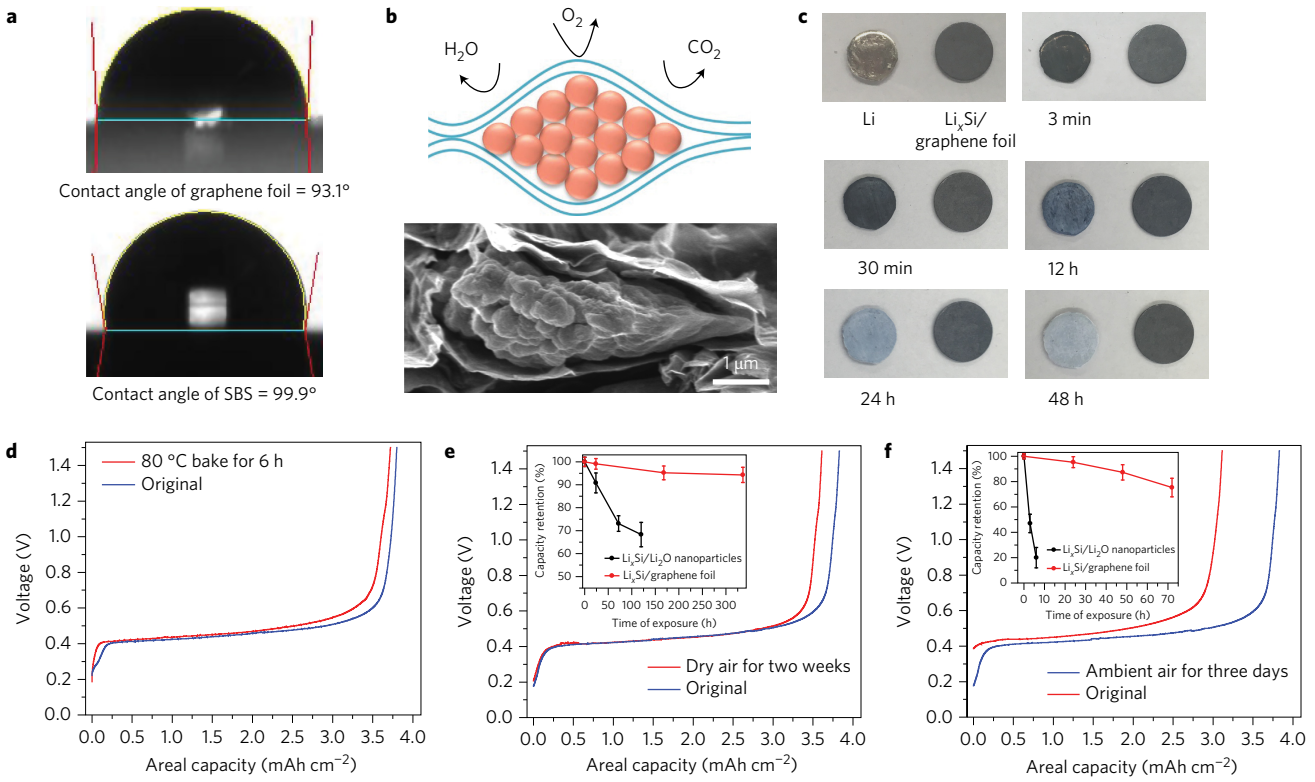


**Figure 3 | Stability of the $Li_xSi$/graphene foil. a**, Images showing the contact angle of a water drop: 93.1° on a graphene foil and 99.9° on a SBS-coated Si wafer. **b**, Top: a schematic illustrating the use of large graphene sheets to prevent the penetration of gas molecules in the air. Bottom: cross-sectional view SEM image confirms that $Li_xSi$ nanoparticles aggregate to form a cluster during calendaring and that the cluster is well encapsulated by large graphene sheets in the hybrid foil. **c**, Photographs of the Li metal and $Li_xSi$/graphene foil exposed to ambient air for different durations. **d**, The areal capacity of a $Li_xSi$/graphene foil before and after baking at 80 °C for 6 h in the dry room (dew point, −50 °C). **e**, The areal capacity retention of a $Li_xSi$/graphene foil in the dry room for two weeks. The inset shows the trend of capacity decay of the $Li_xSi$/graphene foil (red) and $Li_xSi/Li_2O$ nanoparticles (black) with varying durations. For each exposure time, eight cells were fabricated and tested for the $Li_xSi$/graphene foils and $Li_xSi/Li_2O$ nanoparticles, respectively. The error bars indicate the standard deviation of the remaining capacities. **f**, The areal capacity retention of the $Li_xSi$/graphene foil exposed to ambient air for three days. The inset shows the trend of capacity decay of $Li_xSi$/graphene foil (red) and $Li_xSi/Li_2O$ nanoparticles (black) with varying durations. For each exposure time, eight cells were fabricated and tested. The error bars indicate the standard deviation of the remaining capacities for different exposure durations.

and expanded state. The morphology change of individual $Li_xSi$ clusters during cycling is indicated by the cross-sectional SEM images (Fig. 4c). A $Li_xSi$ cluster (~5 μm) is encapsulated by graphene sheets. Void space is created during the delithiation process, which accommodates further volume expansion of the subsequent lithiation process. Therefore, the foil avoids the intrinsic problems of volume expansion that plague alternatives such as Li metal or unlithiated Si. The $Li_xSi$/graphene foil is in the fully charged state and discharged directly to deliver high capacity at the first cycle. Therefore, there is no first cycle CE. The CE of the following cycles is defined as delithiation capacity over lithiation capacity. The second cycle CE is 98.7%, and the CE of the later cycles reaches a high value of 99.92%. The improved early and later cycle CE is ascribed to several characteristics. In the foil, the $Li_xSi$ cluster is enwrapped in graphene sheets, which is chemically and structurally similar to graphite anodes. $Li_xSi$ nanoparticles are packed densely in a cluster form and encapsulated by graphene sheets to lower the surface accessible to the electrolyte and therefore reduces the side reactions.

The excellent performance of the $Li_xSi$/graphene foil in half cells makes it possible to be used in full cells. We paired our $Li_xSi$/graphene foil with a traditional $LiFePO_4$ cathode ($LiFePO_4$:conductive carbon (Super P):polyvinylidene fluoride (PVDF) = 70:20:10 by weight). Figure 4d shows the voltage profiles of foil-$LiFePO_4$ and Li-$LiFePO_4$ cells between 2.5 and 3.8 V. The voltage drop of the full cell is due to the higher voltage plateau (~0.4 V) of $Li_xSi$. The full and half cells show similar capacities of 132.2 mAh g$^{-1}$ and 130.6 mAh g$^{-1}$ at 1 C (the capacity and rate are both based on the mass of $LiFePO_4$). The rate capability was tested at various rates from 0.2 to 20 C (Fig. 4e). At low rate, the capacities of $LiFePO_4$ in full and half cells are similar. Compared with half cells, $LiFePO_4$ in the full cell exhibits higher capacity especially at a high rate (~91.7 mAh g$^{-1}$ at 10 C and 84.0 mAh g$^{-1}$ at 20 C). Both cells exhibit stable cycling for 200 cycles at 1 C (Supplementary Fig. 9). The average CE of the full cell is 99.92%, slightly higher than the half cell (99.84%). After cycling, cells were dissembled to check the morphology of the $Li_xSi$/graphene foil and the Li counter electrode. As shown in Supplementary Fig. 10, Li metal cracks and the superficial Li even peels off after 200 cycles, due to the uncontrolled Li stripping/plating. The magnified SEM image shows massive dendrite formation on the Li metal. The morphology of the $Li_xSi$/graphene foil remains almost the same. The XPS spectra before and after sputtering confirms that the solid electrolyte interphase formed on the Li metal is thick and mainly consists of $Li_2CO_3$ and LiF (Supplementary Fig. 11)[41,42]. In contrast, XPS performed on the foil mainly detects signals from the electrolytes. The $Li_xSi$/graphene foil can also be paired with a $V_2O_5$ cathode ($V_2O_5$ nanosheets:Super P:PVDF = 70:20:10 by weight), exhibiting stable cycling performance at a capacity around 365 mAh g$^{-1}$ at 1 C (the capacity is based on the mass of $V_2O_5$ in the cathode; 1 C = 441 mA g$^{-1}$ of $V_2O_5$; the mass ratio of anode to cathode is 1:4; Supplementary Fig. 12). With an average voltage of 2.5 V, the estimated energy density is ~510 Wh kg$^{-1}$.

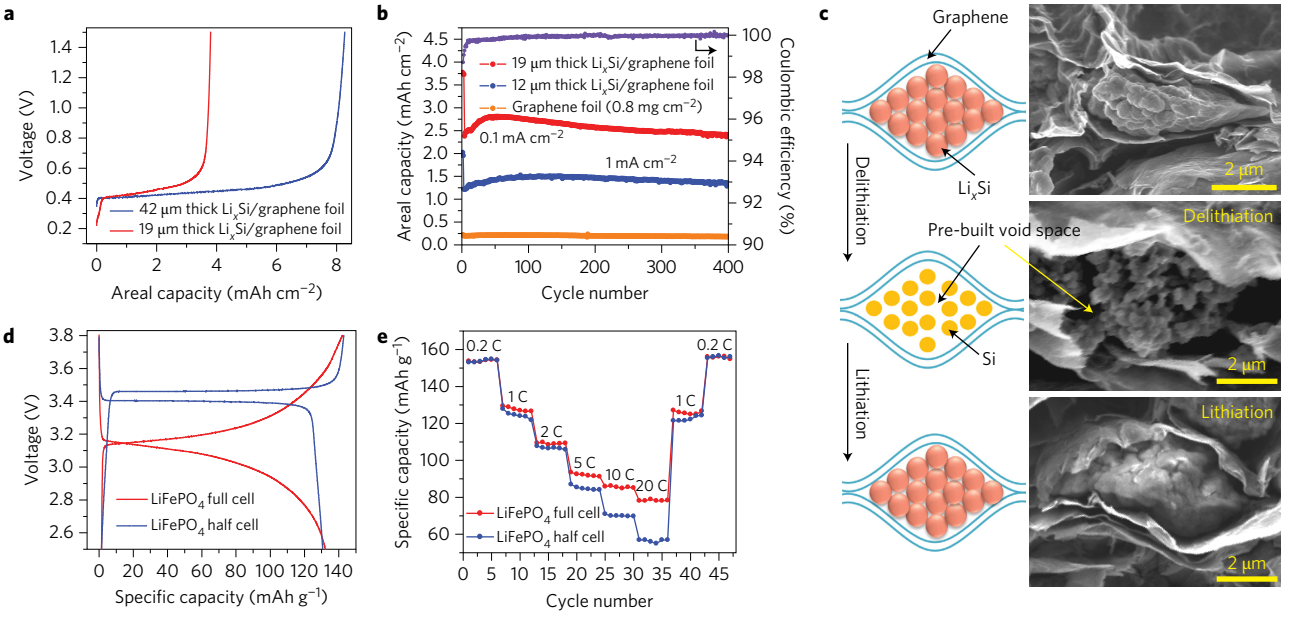


**Figure 4 | Electrochemical performance of the $Li_xSi$/graphene foil. a**, First-cycle areal delithiation capacities of $Li_xSi$/graphene foils with thicknesses of 19 and 42 μm. **b**, Half-cell cycling performance of $Li_xSi$/graphene foils with thicknesses of 12 and 19 μm at 0.1 mA $cm^{-2}$ for the first three cycles and 1 mA $cm^{-2}$ for the following cycles. The orange curve is the cycling performance of a pure graphene foil at the rate of C/5 (1 C = 372 mA $g^{-1}$ of carbon). The Coulombic efficiency is plotted for the foil with the thickness of 19 μm only (purple). **c**, Schematics and the corresponding cross-sectional view SEM images of the foil before and after being cycled and stopped at the delithiated and lithiated states. **d**, The voltage profiles of $Li_xSi$/graphene foil–$LiFePO_4$ full cell and Li–$LiFePO_4$ ($LiFePO_4$:Super P:PVDF = 70:20:10 by weight) half cell within a potential window of 2.5–3.8 eV. The capacity and rate are both based on the mass of $LiFePO_4$ in the cathode. **e**, Rate capability of $Li_xSi$/graphene foil–$LiFePO_4$ and Li–$LiFePO_4$ cells at various rates from 0.2 to 20 C (1 C = 170 mA $g^{-1}$ of $LiFePO_4$).

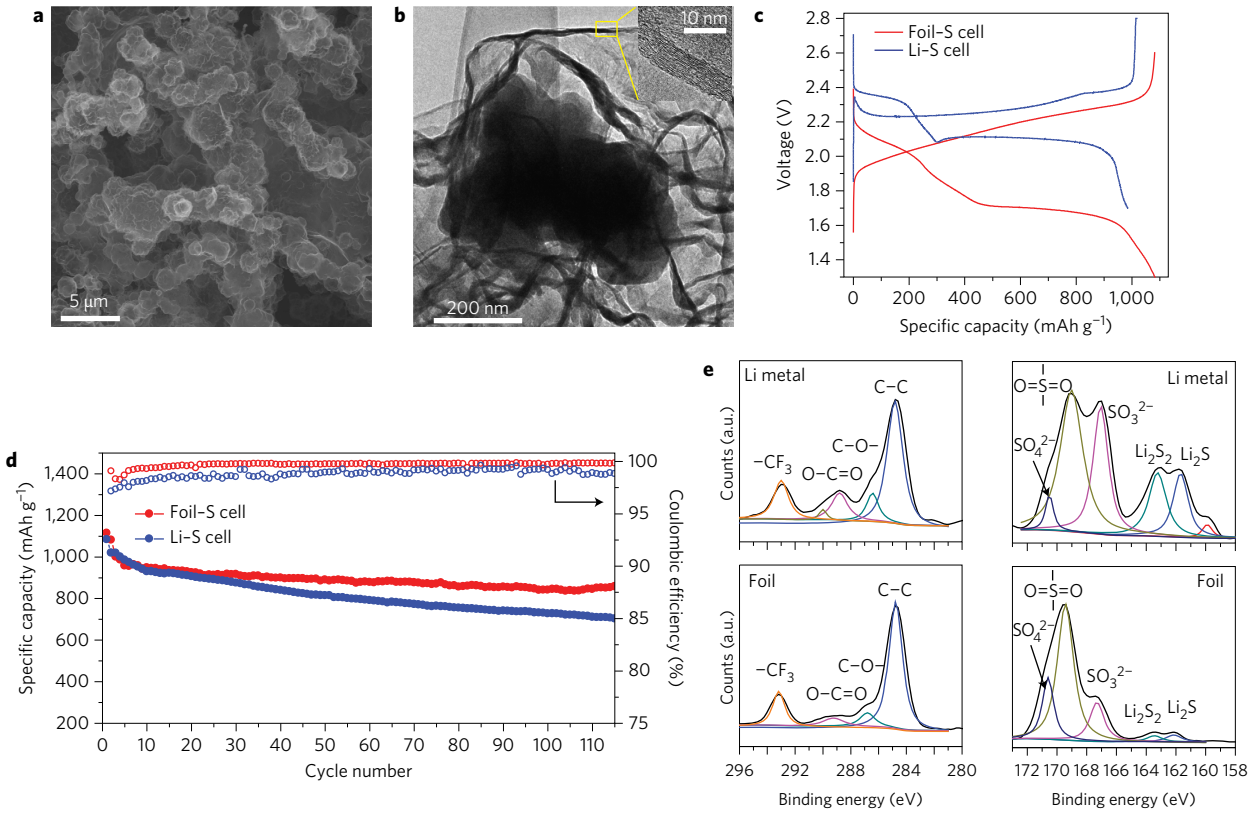


**Figure 5 | Characterization of the sulfur electrode and the sulfur batteries. a**, SEM image of the graphitic carbon-encapsulated sulfur composites. **b**, TEM image of the graphitic carbon-encapsulated sulfur composite. Inset shows the magnified graphitic carbon lattice fringes. **c**, The voltage profiles of $Li_xSi$/graphene foil–S and Li–S cells at a rate of 0.5 C (1 C = 1.67 A $g^{-1}$ of S; the capacity is based on the mass of graphitic carbon-encapsulated S in the cathode; the mass ratio of anode to cathode is 1.8:1). **d**, Cycling performance of $Li_xSi$/graphene foil–S and Li–S cells at a rate of 0.5 C. The Coulombic efficiency is plotted on the right *y* axis. **e**, XPS spectra of C 1s (left) and S 2*p* (right) performed on Li metal (top) and the $Li_xSi$/graphene foil (bottom) cycled in the sulfur batteries for 50 times.

## Characterization of the sulfur batteries

SEM of the graphitic carbon-encapsulated sulfur composite indicates sulfur can permeate into the graphitic carbon cage by capillary force and the composite maintains the original morphology of the cage (Fig. 5a). TEM confirms that the sulfur particles are well encapsulated by the graphitic carbon shell (>20 layers; Fig. 5b). The XRD pattern shows sharp and strong sulfur diffraction peaks (PDF no. 00-08-0247; Supplementary Fig. 13a). The broad peak between 23° and 30° is ascribed to the graphitic carbon cage. Figure 5c shows the voltage profile of the $Li_xSi$/graphene foil–S cell between 1.3 and 2.6 V, which shows a specific capacity of 1,086 mAh $g^{-1}$ with an average voltage of ~1.8 V (the capacity is based on the mass of graphitic carbon-encapsulated S in the cathode). The mass ratio of anode to cathode is 1.8:1. Therefore, the estimated energy density is around 490 Wh $kg^{-1}$. There are two discharge voltage plateaus at 2.1 and 1.7 V, which agree with the Li–S discharge plateaus (2.4 and 2.1 V) and Li–Si (0.4 V) in half cells[43]. The foil–S cell (Fig. 5d) demonstrates excellent cycling stability at 0.5 C and maintains a capacity of 858 mAh $g^{-1}$ after 110 cycles with a CE of 99.5%, higher than that of the half cell (98.8%), indicating its great potential to replace Li metal in sulfur batteries (1 C = 1,672 mA $g^{-1}$ of S). In the Li–S cell, the highly soluble polysulphides can easily diffuse from cathode to anode, and form a deposit of $Li_2S_2$/$Li_2S$ on the Li metal, which is confirmed by the XPS spectrum of S 2*p* (Fig. 5e)[38,42]. The counts of $Li_2S_2$ and $Li_2S$ peaks are highly suppressed for the foil, which indicates that the protective action of the chemically stable graphene sheets minimizes the shuttle effect significantly. The relatively lower peaks of O–C=O and $SO_3^{2-}$ confirms that the decomposition of Li salt is also suppressed in the foil–S cell. Without passivation with the $LiNO_3$ additive, the foil–S cell loses 57% capacity after 110 cycles and consistently exhibits lower CE, which confirms the necessity of the $LiNO_3$ additive in the foil–S cells (Supplementary Fig. 13b).

Finally, we would like to emphasize that the whole foil preparation process is applicable to other materials. $Li_xM$ was synthesized by heating a mixture of M nanoparticles and Li metal under an inert atmosphere. Although M refers to Sn and Al (and Si in our previous example), other materials that form alloys with Li can be potentially used. The $Li_xM$/graphene foil is prepared via vacuum filtration of a suspension of $Li_xM$ and graphene sheets in toluene. The slurry coating and peeling-off approach mentioned above is also suitable. The XRD pattern of the $Li_xSn$/graphene foil indicates that it is made of $Li_{22}Sn_5$ (PDF no. 01-081-6569) and graphitic carbon (Supplementary Fig. 14). The XRD pattern of the $Li_xAl$/graphene foil confirms the existence of $Li_3Al_2$ (PDF no. 04-007-1619) and graphitic carbon. The $Li_xSn$/graphene foil and $Li_xAl$/graphene foil deliver high areal capacities of 2 mAh $cm^{-2}$ and 2.5 mAh $cm^{-2}$, respectively (Supplementary Fig. 15). The $Li_xM$/graphene foils exhibit stable cycling at C/20 for the first three cycles and at C/2 for the following cycles (1C = 990 mA $g^{-1}$ of Sn for the $Li_xSn$/graphene foil, 1C = 2.2 A $g^{-1}$ of Al for the $Li_xAl$/graphene foil). The excellent cycling stability is attributed to the similar structure of fully expanded $Li_xM$ being confined in the highly conductive graphene matrix (Supplementary Fig. 16a). After exposure to ambient air for three days, the $Li_xSn$/graphene and $Li_xAl$/graphene foils exhibit high capacity retention of 91% and 88%, respectively (Supplementary Fig. 16b).

## Conclusions

In this work, we have developed a facile process to fabricate large-scale and freestanding $Li_xM$/graphene anodes with the unique foil structure comprising densely packed $Li_xM$ nanoparticles encapsulated by large graphene sheets. M refers to Si, Sn, and Al, but other materials that can form alloys with Li can potentially be used. With its long-term cyclability and high CE in half cells, the $Li_xSi$/graphene foil has been successfully paired with high-capacity Li-free cathodes (sulfur and $V_2O_5$) to achieve stable full-cell cyclability. The $Li_xM$/graphene foil is highly stable in different air conditions due to its unique structure in which each $Li_xM$ cluster is completely surrounded and protected by the large graphene sheets. The air-stability could be further improved by atomic layer deposition of oxides or fluorides on the double sides of the foils. By addressing the electrochemical and environmental stability simultaneously, our Li-containing anodes should be attractive alternatives to Li metal anodes.

## Methods

Methods and any associated references are available in the online version of the paper.

Received 30 November 2016; accepted 6 June 2017; published online 10 July 2017

## References


1. Chu, S. & Majumdar, A. Opportunities and challenges for a sustainable energy future. *Nature* **488,** 294–303 (2012).
2. Armand, M. & Tarascon, J. M. Building better batteries. *Nature* **451,** 652–657 (2008).
3. Yoshio, M., Wang, H. Y., Fukuda, K., Hara, Y. & Adachi, Y. Effect of carbon coating on electrochemical performance of treated natural graphite as lithium-ion battery anode material. *J. Electrochem. Soc.* **147,** 1245–1250 (2000).
4. Obrovac, M. N. & Chevrier, V. L. Alloy negative electrodes for Li-ion batteries. *Chem. Rev.* **114,** 11444–11502 (2014).
5. Shi, F. F. *et al.* Failure mechanisms of single-crystal silicon electrodes in lithium-ion batteries. *Nat. Commun.* **7,** 11886 (2016).
6. Chan, C. K. *et al.* High-performance lithium battery anodes using silicon nanowires. *Nat. Nanotech.* **3,** 31–35 (2008).
7. Son, I. H. *et al.* Silicon carbide-free graphene growth on silicon for lithium-ion battery with high volumetric energy density. *Nat. Commun.* **6,** 7393 (2015).
8. Liu, N. *et al.* A pomegranate-inspired nanoscale design for large-volume-change lithium battery anodes. *Nat. Nanotech.* **9,** 187–192 (2014).
9. Wang, J. Z., Zhong, C., Chou, S. L. & Liu, H. K. Flexible free-standing graphene-silicon composite film for lithium-ion batteries. *Electrochem Commun.* **12,** 1467–1470 (2010).
10. Zhu, Y. H. *et al.* Directing silicon-graphene self-assembly as a core/shell anode for high-performance lithium-ion batteries. *Langmuir* **29,** 744–749 (2013).
11. Cui, L. F., Hu, L. B., Choi, J. W. & Cui, Y. Light-weight free-standing carbon nanotube-silicon films for anodes of lithium ion batteries. *ACS Nano* **4,** 3671–3678 (2010).
12. Wu, X. L. *et al.* Carbon-nanotube-decorated nano-$LiFePO_4$@C cathode material with superior high-rate and low-temperature performances for lithium-ion batteries. *Adv. Energy Mater.* **3,** 1155–1160 (2013).
13. Wang, L. *et al.* Crystal orientation tuning of $LiFePO_4$ nanoplates for high rate lithium battery cathode materials. *Nano Lett.* **12,** 5632–5636 (2012).
14. Ji, X. L., Lee, K. T. & Nazar, L. F. A highly ordered nanostructured carbon-sulfur cathode for lithium-sulfur batteries. *Nat. Mater.* **8,** 500–506 (2009).
15. Liu, Y. Y. *et al.* $V_2O_5$ nano-electrodes with high power and energy densities for thin film Li-ion batteries. *Adv. Energy Mater.* **1,** 194–202 (2011).
16. Jin, S. *et al.* Covalently connected carbon nanostructures for current collectors in both the cathode and anode of Li–S batteries. *Adv. Mater.* **28,** 9094–9102 (2016).
17. Shen, C. F. *et al.* Silicon(lithiated)-sulfur full cells with porous silicon anode shielded by Nafion against polysulfides to achieve high capacity and energy density. *Nano Energy* **19,** 68–77 (2016).
18. Xu, W. *et al.* Lithium metal anodes for rechargeable batteries. *Eng. Environ. Sci.* **7,** 513–537 (2014).
19. Kim, H. *et al.* Metallic anodes for next generation secondary batteries. *Chem. Soc. Rev.* **42,** 9011–9034 (2013).
20. Aurbach, D., Zinigrad, E., Cohen, Y. & Teller, H. A short review of failure mechanisms of lithium metal and lithiated graphite anodes in liquid electrolyte solutions. *Solid State Ion.* **148,** 405–416 (2002).
21. Chandrashekar, S. *et al.* $^7$Li MRI of Li batteries reveals location of microstructural lithium. *Nat. Mater.* **11,** 311–315 (2012).
22. Xu, K. Nonaqueous liquid electrolytes for lithium-based rechargeable batteries. *Chem. Rev.* **104,** 4303–4417 (2004).
23. Liang, Z. *et al.* Composite lithium metal anode by melt infusion of lithium into a 3D conducting scaffold with lithiophilic coating. *Proc. Natl Acad. Sci. USA* **113,** 2862–2867 (2016).
24. Lin, D. C. *et al.* Layered reduced graphene oxide with nanoscale interlayer gaps as a stable host for lithium metal anodes. *Nat. Nanotech.* **11,** 626–632 (2016).
25. Mogi, R. *et al.* Effects of some organic additives on lithium deposition in propylene carbonate. *J. Electrochem. Soc.* **149,** 1578–1583 (2002).

26. Ding, F. *et al.* Dendrite-free lithium deposition via self-healing electrostatic shield mechanism. *J. Am. Chem. Soc.* **135,** 4450–4456 (2013).
27. Yan, K. *et al.* Ultrathin two-dimensional atomic crystals as stable interfacial layer for improvement of lithium metal anode. *Nano Lett.* **14,** 6016–6022 (2014).
28. Kazyak, E., Wood, K. N. & Dasgupta, N. P. Improved cycle life and stability of lithium metal anodes through ultrathin atomic layer deposition surface treatments. *Chem. Mater.* **27,** 6457–6462 (2015).
29. Yan, K. *et al.* Selective deposition and stable encapsulation of lithium through heterogeneous seeded growth. *Nat. Energy* **1,** 16010 (2016).
30. Kozen, A. C. *et al.* Next-generation lithium metal anode engineering via atomic layer deposition. *ACS Nano* **9,** 5884–5892 (2015).
31. Xiang, B., Wang, L., Liu, G. & Minor, A. M. Electromechanical probing of Li/$Li_2CO_3$ core/shell particles in a TEM. *J. Electrochem. Soc.* **160,** 415–419 (2013).
32. Wang, Z. H. *et al.* Application of stabilized lithium metal powder (SLMP (R)) in graphite anode—a high efficient prelithiation method for lithium-ion batteries. *J. Power Sources* **260,** 57–61 (2014).
33. Qian, J. F. *et al.* High rate and stable cycling of lithium metal anode. *Nat. Commun.* **6,** 6362 (2015).
34. Stankovich, S. *et al.* Synthesis of graphene-based nanosheets via chemical reduction of exfoliated graphite oxide. *Carbon* **45,** 1558–1565 (2007).
35. Zang, J. F. *et al.* Multifunctionality and control of the crumpling and unfolding of large-area graphene. *Nat. Mater.* **12,** 321–325 (2013).
36. Bunch, J. S. *et al.* Impermeable atomic membranes from graphene sheets. *Nano Lett.* **8,** 2458–2462 (2008).
37. Zhao, J. *et al.* Dry-air-stable lithium silicide–lithium oxide core–shell nanoparticles as high-capacity prelithiation reagents. *Nat. Commun.* **5,** 5088 (2014).
38. Zhou, G. M. *et al.* A graphene-pure-sulfur sandwich structure for ultrafast, long-life lithium-sulfur batteries. *Adv. Mater.* **26,** 625–631 (2014).
39. Li, X. S. *et al.* Large-area synthesis of high-quality and uniform graphene films on copper foils. *Science* **324,** 1312–1314 (2009).
40. Cambaz, Z. G., Yushin, G., Osswald, S., Mochalin, V. & Goyotsi, Y. Noncatalytic synthesis of carbon nanotubes, graphene and graphite on SiC. *Carbon* **46,** 841–849 (2008).
41. Aurbach, D., Weissman, I., Schechter, A. & Cohen, H. X-ray photoelectron spectroscopy studies of lithium surfaces prepared in several important electrolyte solutions. A comparison with previous studies by Fourier transform infrared spectroscopy. *Langmuir* **12,** 3991–4007 (1996).
42. Li, W. *et al.* The synergetic effect of lithium polysulfide and lithium nitrate to prevent lithium dendrite growth. *Nat. Commun.* **6,** 7436 (2015).
43. Seh, Z. W. *et al.* Sulfur–$TiO_2$ yolk–shell nanoarchitecture with internal void space for long-cycle lithium–sulfur batteries. *Nat. Commun.* **4,** 1331 (2013).


## Acknowledgements

Y.C. acknowledges the support from the Assistant Secretary for Energy Efficiency and Renewable Energy, Office of Vehicle Technologies, Battery Materials Research Program of the US Department of Energy. Y.L. acknowledges the National Science Foundation Graduate Fellowship Program.

## Author contributions

J.Z., G.Z. and Y.C. conceived the concept. J.Z. and G.Z. carried out the synthesis and performed materials characterization and electrochemical measurements. J.X., Y.J., L.L., Y.L., P.-C.H. and J.W assisted in the synthesis and characterization of electrode materials. K.L. conducted stress–strain tests. K.Y. and H.-M.C. provided important experimental insights. J.Z., G.Z., K.Y., Y.L., H.-M.C. and Y.C. co-wrote the paper. All authors discussed the results and commented on the manuscript.

## Additional information

Supplementary information is available in the online version of the paper. Reprints and permissions information is available online at www.nature.com/reprints. Publisher's note: Springer Nature remains neutral with regard to jurisdictional claims in published maps and institutional affiliations. Correspondence and requests for materials should be addressed to Y.C.

## Competing financial interests

The authors declare no competing financial interests.

## Methods

**Preparation of the $Li_xM$/graphene foils.** M represents Si, Al, Sn and other materials that can form alloys with Li. M nanoparticles (Si nanoparticles (100 nm, MTI Inc.), Al nanoparticles (50 nm, MTI Inc.) and Sn nanoparticles (<150 nm, Sigma-Aldrich)) were dried under vacuum for 48 h to remove trapped water. $Li_xM$ was prepared by mechanically stirring a stoichiometric mixture of M nanoparticles and Li metal foil at 250 °C for 48 h in a glove box filled with argon ($H_2O$ level <0.1 ppm and $O_2$ level <1.0 ppm). The synthesis temperature of $Li_xSn$ is slightly different, maintained between the melting points of Li metal and Sn to ensure the preservation of the morphology of the Sn nanoparticles. The graphene sheets were fabricated by an intercalation–expansion–exfoliation method, in which graphene sheets were exfoliated via a graphite intercalation compound with negligible oxidation as described in ref. 38. The $Li_xM$ alloy was mixed with graphene sheets and SBS (Kraton D1161) rubber (80:10:10 by weight) in anhydrous toluene to form a slurry, which was then cast on a commercial PET release film. After drying, it was peeled off as a large freestanding $Li_xM$/graphene foil. $Li_xM$/graphene foils were also prepared via vacuum filtration of a suspension of $Li_xM$ and graphene sheets (80:20 by weight) in anhydrous toluene. In case there were unprotected $Li_xM$ nanoparticles on the surface of the foil, thin layers of graphene sheets were coated on the double sides of the foil to further enhance the protection. After drying, a pressure of 40 MPa was applied to the foil and held for 0.5 h. The whole foil preparation process was performed under argon atmosphere.

**Electrochemical testing.** For the $Li_xM$/graphene foil half cells, the working electrodes were assembled in 2032-type coin cells with Li metal (Alfa Aesar) as the counter electrode. The electrolyte was 1.0 M $LiPF_6$ in 1:1 v/v ethylene carbonate/diethyl carbonate (BASF, LP40) with 10 vol% fluoroethylene carbonate and 1 vol% vinylene carbonate. After a cell was assembled, it took about 6 h for the electrode to reach equilibrium as determined by the stabilized voltage of the cell. For the fabrication of the $LiFePO_4$ cathode, a $LiFePO_4$ slurry ($LiFePO_4$ (MTI Inc.):Super P (TIMCAL):PVDF (Kynar HSV 900)) = 70:20:10 by weight) was coated onto an Al foil and dried under vacuum. The total mass loading was ~10 mg $cm^{-2}$. In the foil–$LiFePO_4$ cell, the mass ratio of anode to cathode is 1:5. For the fabrication of the $V_2O_5$ cathode, a $V_2O_5$ slurry ($V_2O_5$ nanosheets:Super P:PVDF = 70:20:10 by weight) was coated onto an Al foil and dried under vacuum. For the fabrication of the graphitic carbon-encapsulated sulfur electrodes, a sulfur slurry (graphitic C-encapsulated S:Super P:PVDF = 70:20:10 by weight) was coated on an Al foil and dried under vacuum. The mass loading of the sulfur cathode was ~1 mg $cm^{-2}$. The electrolyte was 1.0 M lithium bis-trifluoromethanesulphonylimide in 1:1 v/v 1,3-dioxolane/1,2-dimethoxyethane with 0.4 M $LiNO_3$ additive. In the foil–S cell, the mass ratio of anode to cathode is 1.8:1. Galvanostatic cycling was carried out using an MTI 8-channel battery tester and the voltage depends on the specific cell. For the full-cell performance, rate and capacity are both based on the mass of active cathode materials. After assembly of the $Li_xSi$/graphene foil–S cell, the cell was in the charged state. For the calculation of the CE, the first discharge capacity was ignored. The second CE = $\text{capacity}_{2\text{nd discharge}}/\text{capacity}_{1\text{st charge}} \times 100\%$.

**Characterizations.** Powder X-ray diffraction was performed on a PANalyticalX'Pert with Ni-filtered Cu Kα radiation. XPS analysis was performed on PHI Versa Probe 5000 (Physical Electronics). SEM images were taken using a FEI XL30 Sirion SEM. The TEM images were acquired using FEI Titan 80–300 environmental TEM at an acceleration voltage of 80 kV. The stress–strain tests were performed on TA Instrument Q800 dynamic mechanical analyser.

**Data availability.** The data that support the plots within this paper and other finding of this study are available from the corresponding author upon reasonable request.